Recrystallization and texture evolution of cold pilgered FeCrAl cladding tube during annealing at 700 °C□1000 °C

Journal of Nuclear Materials 577 (2023) 154303

Contents lists available at ScienceDirect

Journal of Nuclear Materials

journal homepage: www.elsevier.com/locate/jnucmat

Recrystallization and texture evolution of cold pilgered FeCrAl cladding tube during annealing at 700 °C∼1000 °C

Xiao Qin[a,c], Ruiqian Zhang[b], Peinan Du[b], Jingyuan Pei[b], Qianfu Pan[b], Yu Cao[c], Huiqun Liu[a,*]

[a] School of Materials Science and Engineering, Central South University, Changsha 410083, China
[b] Science and Technology on Reactor Fuel and Materials Laboratory, Nuclear Power Institute of China, Chengdu, Sichuan 610213, China
[c] Department of Industrial and Materials Science, Chalmers University of Technology, Gothenburg 41296, Sweden

ARTICLE INFO

Article history:
Received 26 October 2022
Revised 26 January 2023
Accepted 30 January 2023
Available online 3 February 2023

Keywords:
Recrystallization
FeCrAl cladding
Laves precipitates
EBSD
Texture

ABSTRACT

FeCrAl alloys are being developed as potential accident-tolerant fuel cladding materials for the light water reactors due to significantly improved steam oxidation and good mechanical properties at high temperatures. In this study, the recrystallization and texture evolution of the cold pilgered FeCrAl cladding tube was investigated by means of hardness measurements and electron backscatter diffraction (EBSD) during annealing at 700∼1000 °C. The partially recrystallized maps were deconstructed into deformed, recovered, and recrystallized grain fractions based on the critical internal misorientation angle. In the early stages of recrystallization, cold pilgered cladding tubes contained a mixture of discontinuously recrystallized {111}<110> newly nucleated grains and heterogeneous deformed ⟨110⟩ orientation grains. The deformed microstructural inhomogeneity state could be explained based on the Taylor factor. The rate of recrystallization increased with increasing annealing temperature, which was described by the Johnson-Mehl-Avrami-Kolmogorov equation. The cladding tube showed slow recrystallization kinetics and thermally stable grains due to the pinning of the grain boundaries by the Laves precipitates. The dominant α-fiber decreased and γ-fiber increased with increasing recrystallization fraction in the cold pilgered tubes. The high area fraction and stable γ-fiber would be beneficial to the processability of the cladding tube.

1. Introduction

The fuel cladding tube, as the second barrier for the safe operation of nuclear reactors, suffers from the risk of failure due to long-term exposure to high-temperature steam oxidation, corrosion, irradiation and even lack of coolant for a long time [1,2]. In the Fukushima nuclear accident in 2011, the lack of circulating cooling caused a violent reaction between commercial zirconium alloys and high-temperature steam to generate explosive hydrogen, which resulted in the failure of the cladding tube [3–6]. Therefore, researchers proposed to design an accident-tolerant fuel (ATF) material to improve the safety margin of the cladding tube [7–9]. In recent years, FeCrAl alloys have been considered one of the most promising ATF materials due to their excellent high-temperature steam oxidation resistance [10,11]. Based on the ATF concept, 10∼13%wt Cr and 4∼6%wt Al were used to control the microstructure and processability of FeCrAl alloys [7,9]. The addition of Y element improved the adhesion of the α-Al_2O_3 oxide protective layer [12,13], in addition, Mo, Nb and Ta were aimed at the solid solution and precipitation strengthening the Fe-bcc matrix and optimizing microstructure [8,14,15].

The FeCrAl fuel cladding tube requires a seamless tube with an outer diameter of ∼9.5 mm and a wall thickness of ∼0.4 mm to compensate for the neutron economy [1,16]. Cold pilger rolling has large cumulative deformation per pass, which shortens the production cycle and improves production efficiency [17]. The cladding tube with higher performance and reliability requirements is suitable for pilgering method. The cladding tube usually requires one-pass final cold rolling to obtain high dimensional accuracy. The final tube requires annealing to relieve stress and optimize microstructure, which are closely related to the performance of the cladding tube. Therefore, studying the microstructural evolution of cold pilgered cladding tubes during annealing process aims to provide some guidance for the development of commercial FeCrAl cladding tubes.

The recovery, recrystallization and grain coarsening would occur in deformed FeCrAl alloys during annealing process [18]. The recovery and recrystallization during annealing of FeCrAl alloy

* Corresponding author.
E-mail address: liuhuiqun@csu.edu.cn (H. Liu).

https://doi.org/10.1016/j.jnucmat.2023.154303
0022-3115/

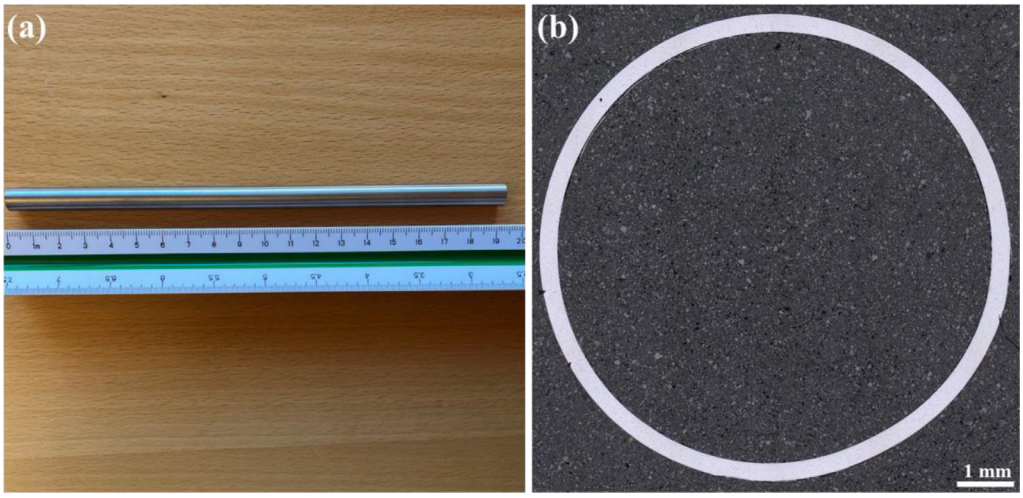

Fig. 1. (a) FeCrAl cladding tube fabricated by cold pilger rolling; (b) cross-section optical micrograph of a FeCrAl tube.

have been reported in different investigations [18–20]. Yamamoto et al. [8] reported that hot-rolled C35MN alloy (Fe-13Cr-4.5Al-0.15Y-2Mo-1Nb) annealed at 800 °C for 24 h could obtain 1∼3 μm subgrains with submicron size Laves phase precipitates on grain boundaries. Sun et al. [18] investigated the recovery and recrystallization of FeCrAl alloys with different Nb contents and found that increasing Nb content stabilizes recovery and recrystallization, which is due to Fe_2Nb Laves phase precipitated at grain boundaries. Liang et al. [20] studied the effect of cold rolling reduction and annealing temperature on the recrystallization of FeCrAl alloy, and the results showed that the increase of deformation and annealing temperature would accelerate the recrystallization process. However, the as-received materials in the above studies focused on FeCrAl plates without reporting cold pilgered cladding tubes fabricated under industrial conditions. Annealing of cold pilgered cladding tubes is crucial for controlling the properties and microstructure of finial tubes. This study could provide a reference for the development of commercial cladding tubes.

In the present study, the recrystallization behavior of cold pilgered FeCrAl cladding tube annealed at 700∼1000 °C was investigated by combining EBSD and hardness tests. For in-depth investigation, the partially recrystallized EBSD map was subdivided into deformed, recovered, and recrystallized grain fractions. The microstructure and texture evolutions occurring during recrystallization are detailed by comparing the morphological information with grain size and boundary misorientation. This research method that quantifies the evolution of recrystallization would help to design rational annealing schemes to balance properties and microstructure.

2. Experimental procedures

The FeCrAl alloy investigated in this work was provided by the Nuclear Power Institute of China. The nominal chemical composition of the alloy was 13Cr-4.5Al-2Mo-1Nb-0.4Ta-0.05Y (wt.%). The FeCrAl HIPed (hot isostatic pressed) ingot billet was subjected to homogenization and solution treatment, followed by hot extrusion and pilger rolling with a thickness reduction of ∼40% for four times to obtain cold pilgered cladding tube. Each pass of pilgered tube blank was annealed at 800 °C for 30 min to reduce stress and defects and prevent premature cracking during rolling. The as-received sample is the cold pilgered thin-wall tube with an outer diameter of ∼9.5 mm and a wall thickness of ∼0.38 mm. Fig. 1 shows macroscopic and cross-section optical images of the cladding tube.

The cold pilgered FeCrAl cladding tube was cut into two semicircular tubes with a length of 10 mm along the tube axis direction by electrical discharge machining. Then specimens were individually isothermally annealed at different temperatures ranging from 700 °C to 1000 °C for 30 min to investigate the starting recrystallization temperature. Afterward, different small samples were subjected to isothermal annealing at three different temperatures for different time spans to evaluate the thermal stability, recrystallization and texture evolution of the cladding tube.

The metallographic samples were mounted in conductive resin and then fine grinding to 1000# with SiC sandpaper, and finally polished with 0.06 μm colloidal silica. RD and ND correspond respectively to axial and radial directions of the tube. Vickers hardness measurements were performed on the longitudinal plane (RD-ND) using a 1 kgf load with 15 s dwell time. The reported hardness values HV1±ΔHV1 were the average of 7 indentations with the standard deviation ΔHV1 from the average. EBSD data were collected using a JEOL 7900F FE-scanning electron microscope (FE-SEM) coupled with an Oxford C-nano EBSD detector operating at 20 kV, with a step size of 1.2 μm.

EBSD analysis was performed with the commercial software HKL* Channel 5. The EBSD maps were filled with zero solutions by extrapolation up to six neighbors. The Tango tool in Channel 5 software was used to identify and reconstruct subgrains and grains based on the threshold misorientation angle of 2° and 15°, respectively. Subgrains were bounded by a low-angle boundary (LAGBs, $2° \leqslant \theta < 15°$) and grains only surrounded by a high-angle boundary (HAGBs, $\theta \geqslant 15°$). For a detailed discussion of the evolution of microstructure and texture during recrystallization. Partially recrystallized IPF maps were deconstructed into deformed, recovered, and recrystallized grain fractions, which allow individual subsets to quantify the contribution of each fraction to the whole. By employing the cut-off criterion i.e., critical internal misorientation angle (θ_c), the microstructure can be separated into the following units: (i) structures with internal misorientations above θ_c, (ii) features with internal average misorientation angle below θ_c, but the misorientation from subgrain to subgrain is above it, and (iii) structures with internal misorientations below the critical angle. Therefore, units (i) and (ii) clearly belong to the deformed and substructured fractions respectively, all the remaining grains are classified as recrystallized. An orientation tolerance of 15° was used for estimations of the area fractions of fiber texture. The crystallographic texture is expressed by the orientation distribution function (ODF) in Euler space. Texture results were constructed using the spherical harmonics

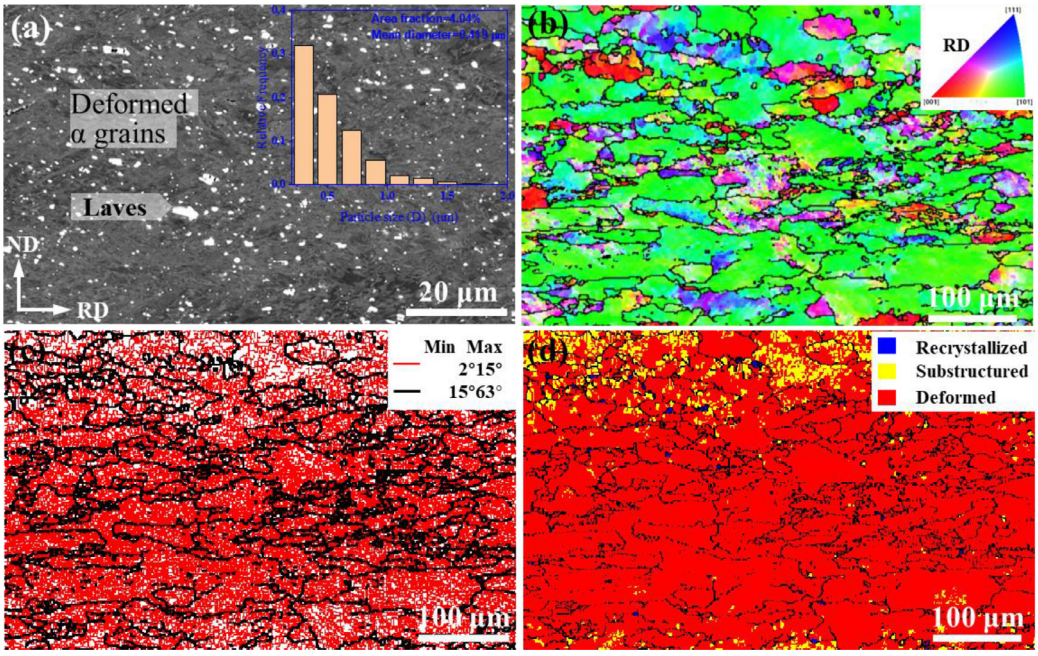

Fig. 2. Microstructures of the as-received cold-pilgered tube, (a) BSE image, (b) IPF map, (c) GB map and (d) RXF map.

method [21] with a series rank of 22 and a Gaussian half-width of 5°

3. Results

3.1. Cold-pilgered microstructure

Fig. 2(a) shows the longitudinal plane SEM-backscattered electron (BSE) image of the as-received cold-pilgered tube. Heterogeneous shear microstructure and numerous Laves precipitates could be observed in the α matrix. Laves precipitates (~419 nm in diameter with an estimated area fraction of 4.04%) were distributed in the deformation bands. Since cold rolling would not cause the formation of Laves precipitates, it indicates that they exist before rolling. These mostly spherical or elliptical Laves precipitates range from tens of nanometers to several micrometers. Cracks within coarse Laves precipitates are occasionally observed due to pilger rolling. The fine Laves precipitates may be due to the fragmentation of coarse Laves precipitates. The inverse pole figure (IPF) map in Fig. 2(b) demonstrates the cold-pilgered microstructure consists of many grains with <110> orientation (in green) parallel to the rolling direction. Indeed, strong deformation texture α-fiber (<110>//RD) often appeared in the rolling process of FeCrAl alloy [18,19]. A large number of deformed grains were elongated, while many fine fragmented grains were also observed. The fragmented grains were surrounded by HAGBs as shown in Fig. 2(c). The high density of LAGBs within deformed grains resulted in the predominance of LAGBs over HAGBs. Fig. 2(d) shows the recrystallization fraction map of the as-received sample with recrystallized grains (blue), substructured grains (yellow) and deformed grains (red). The area fraction of deformed region and substructured region was about 85% and 14%, respectively. The high proportion of deformed structure indicated severe deformation of the cold pilgered tube.

3.2. Recrystallization kinetics

Cold-worked metals usually undergo recovery, recrystallization and grain growth during the annealing process [22]. Mechanical

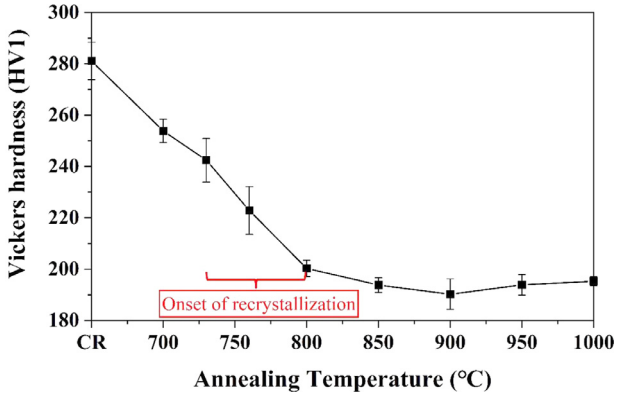

Fig. 3. Variation of Vickers hardness of FeCrAl cladding tube with increasing annealing temperature up to 1000° C.

properties usually show a sharp drop in hardness during recrystallization. To determine the start recrystallization temperature of FeCrAl cold pilgered tube, isochronal 30 min anneals of the tube was carried out at temperatures ranging from 700 °C to 1000 °C. The variation of Vickers hardness with increasing annealing temperature is shown in Fig. 3. Some important points could be understood by considering the hardness variation and EBSD recrystallization fraction maps at different annealing temperatures (Fig. 4). After annealing at 700 °C for 30 min, although the hardness decreased significantly, only deformed region could be observed in Fig. 4(a), indicating that this stage was undergoing recovery. When the temperature increased to 730 °C, the hardness decreased further, and a small number of recrystallized grains (blue area) was observed in Fig. 4(b). The recrystallization fraction increases rapidly with increasing temperature as shown in Fig. 4(c, d). Stable plateaus in hardness appear annealed at 850 ~ 1000 °C, indicating full recrystallization, which could be observed from the recrystallization fraction map. Therefore, we conclude that the start recrystallization temperature of the cold pilgered tube was 730 °C.

To understand the microstructural evolution of cold pilgered tube during annealing, we selected the temperature range of

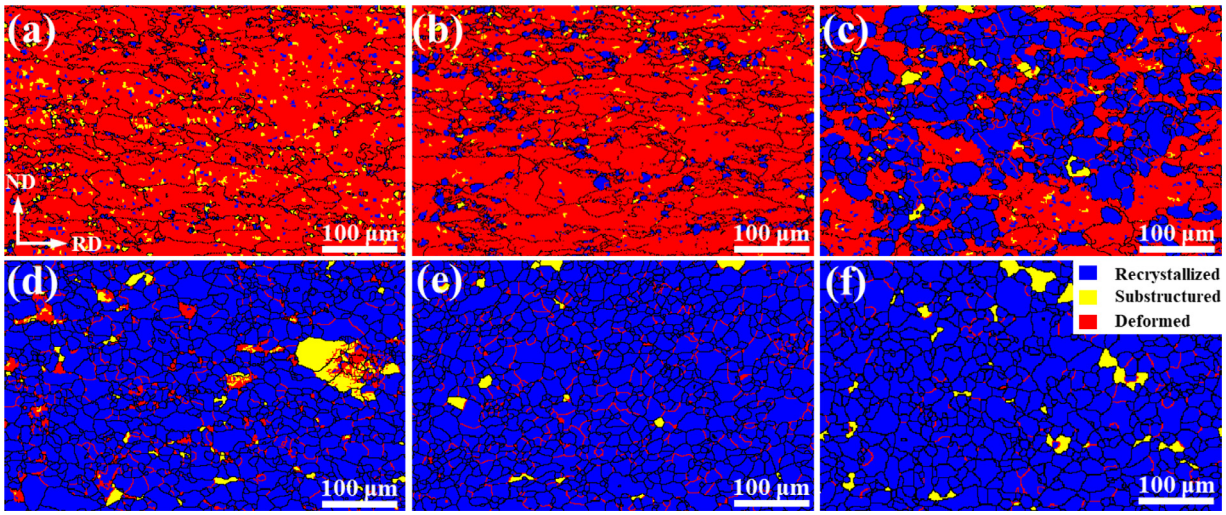

Fig. 4. Determining the recrystallization temperature of cold pligered FeCrAl cladding tube, based on the EBSD recrystallization fraction map including (a) 700 °C, (b) 730 °C, (c) 760 °C, (d) 800 °C, (e) 850 °C and (f) 900°C. The annealing time is 30 min for all the samples.

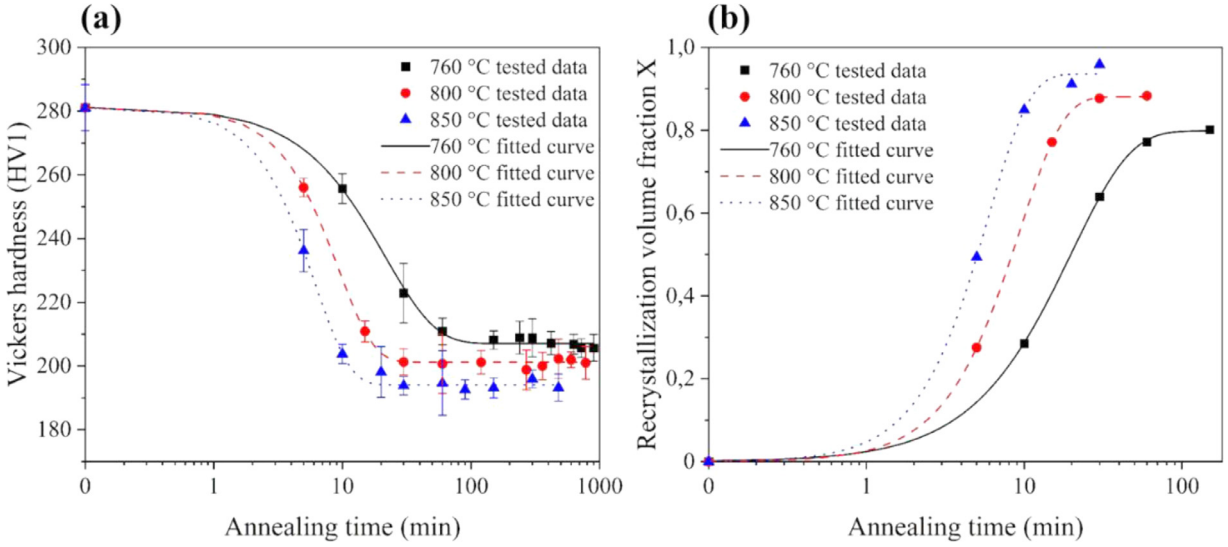

Fig. 5. Variation of (a) Vickers hardness and (b) recrystallization volume fraction of cold pilgered cladding tube annealed at 760 °C, 800 °C and 850 °C for different time.

760~850 °C for different annealing times to study the recrystallization kinetics. The Vickers hardness as a function of annealing time at different temperatures is illustrated in Fig. 5(a). As the annealing time increases, the hardness decreases rapidly from 281±7 HV1 in the cold-rolled state until it reaches a stable plateau. Interestingly, the final stable hardness decreases with increasing annealing temperature. The higher the annealing temperature, the faster the decrease in hardness, indicating that increasing the annealing temperature will accelerate the recrystallization. The variation of hardness versus annealing time exhibited a typical S-shape, following the Johnson–Mehl–Avrami–Kolmogorov (JMAK) model [22,23]. The JMAK equation can be used to quantitatively describe the recrystallization kinetics when nucleation and growth are involved:

$$X_{REX} = 1 - \exp(-kt)^n \quad (1)$$

Where, k is the rate constant, t is the time, and n is the Avrami exponent. Avrami exponent n (values ranging from 1 to 4) reflects the nucleation rate and/or the growth morphology, and k is the pre-exponential factor, a kinetic parameter depending on the annealing temperature, nucleation rate and growth rate. The theoretical value of n is 4, assuming that the nucleation and growth rates remain constant during recrystallization. In fact, the nucleation rate is not a constant but a decreasing function of time. The value of n is 3 for the fact that all nuclei are formed at $t = 0$, i.e. three-dimensional growths. Low n values are for two-dimensional ($n = 2$) and one-dimensional ($n = 1$) growth, respectively.

The recrystallization fraction X_{REX} could also be used to denote the hardness using the relation:

$$X_{REX} = \frac{HV_{CR} - HV_t}{HV_{CR} - HV_{REX}} \quad (2)$$

Here, HV_{CR} is the hardness value after cold pilger rolling, HV_t is the hardness value during annealing time t and HV_{REX} is hardness of the fully recrystallized state.

The recrystallization fraction was obtained from hardness testing using Eq. (2). Recrystallization kinetics measurements were performed by plotting the recrystallization fraction versus annealing time as shown in Fig. 5(b). The incubation time for recrystallization largely decreased with increasing annealing temperature. The values of k and n are obtained by the non-linear fitting, as shown in Table 1. The values of n and k increased with an increase in annealing temperature.

In order to determine the activation energy, the dependence of the time to 50% recrystallized fraction ($t_{X=0.5}$) on annealing tem-

Table 1
Values of k and n for recrystallization kinetics of cold pilgered FeCrAl cladding tube during isothermal annealing at 760, 800 and 850 °C.

Temperature (°C)	760	800	850
k	0.05	0.11	0.17
n	1.2 ± 0.03	1.5 ± 0.02	1.7 ± 0.03

perature can be approximated to describe by the Arrhenius relationship shown:

$$t_{X=0.5} = t_0 \exp\left(\frac{Q_{X=0.5}}{RT}\right) \quad (3)$$

Where, $t_{X=0.5}$ is a constant independent of temperature, $Q_{X=0.5}$ is the apparent activation energy, R is the ideal gas constant ($R = 8.314$ J mol^{-1} K^{-1}) and T is the absolute annealing temperature.

The apparent activation energy, $Q_{X=0.5} = 144.46$ kJ/mol, was determined by plotting ln $t_{X=0.5}$ versus $1/T$, which produces a straight line with a slope $Q_{X=0.5}/R$, as shown in Fig. 6.

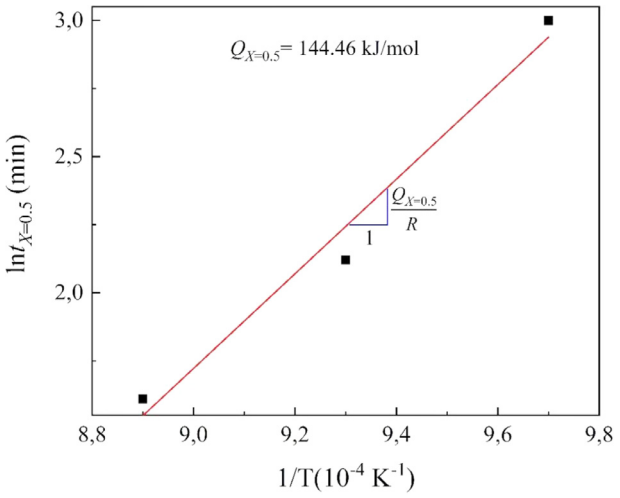

Fig. 6. Arrhenius plot of the rate constant $t_{X=0.5}$ for the recrystallized kinetics of cold pligered cladding tube. Time to $X = 0.5$ is determined from the hardness evolution in dependence on annealing temperature. The data are fitted with a straight line whose slope $Q_{X=0.5}/R$ is proportional to the apparent activation energy $Q_{X=0.5}$.

3.3. Recrystallization microstructure

To study the microstructural evolution during annealing, we selected specific samples with different hardness representing different recrystallization stages. Fig. 7 presents the EBSD IPF maps consisting of recrystallized grains at different annealing stages in FeCrAl cold-pilgered tube. As shown in Fig. 7(a), a small fraction of recrystallized grains (area fraction ~13.5%) were distinguished from the deformed grains in the low-temperature-annealed (730 °C) for 30 min. The recrystallized grains are surrounded by boundaries with orientation angles higher than 15° and the internal structure of deformed grains appears to be composed of many subgrains. The fine recrystallized grains randomly distributed at the grain boundaries indicated that the alloy undergoes discontinuous static recrystallization. Fig. 7(b-d) shows IPF maps of the as-received sample annealed at 760 °C for 30 min, 60 min and 900 min corresponding to the recrystallization area fractions of 57.6%, 76.1% and 80.3%, respectively. The area fraction of recrystallized grains increased with an increase in annealing time. The recrystallized area fraction for annealing for 900 min did not increase significantly compared to annealing for 60 min, and

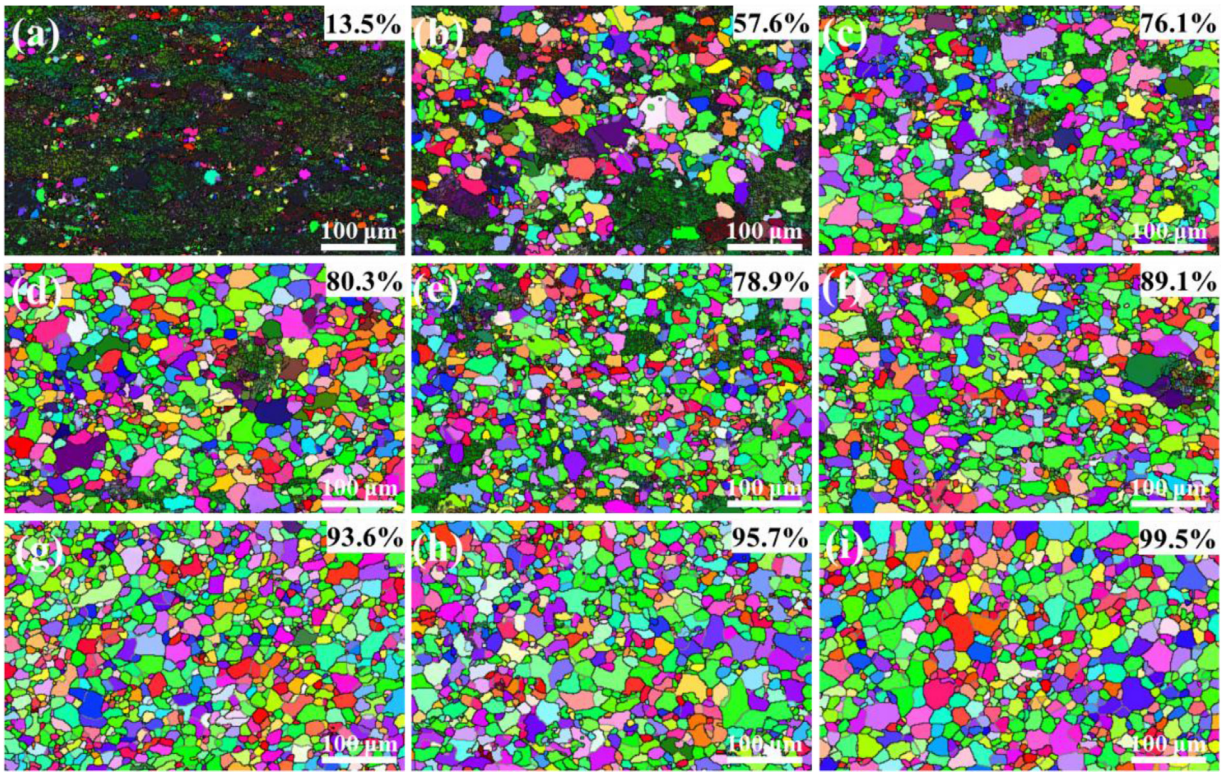

Fig. 7. IPF maps of partially recrystallized tube samples annealed for (a) 30 min at 730 °C, (b) 30 min at 760 °C, (c) 60 min at 760 °C, (d) 900 min at 760 °C, (e) 15 min at 800 °C, (f) 30 min at 800 °C, (g) 30 min at 850 °C, (h) 480 min at 850 °C and (i) 30 min at 1000 °C. HAGBs (with misorientation angles higher than 15°) shown as black lines and LAGBs (with misorientation angles between 2° and 15°) shown as gray lines. Dark region=un-recrystallized grains and light region=recrystallized grains.

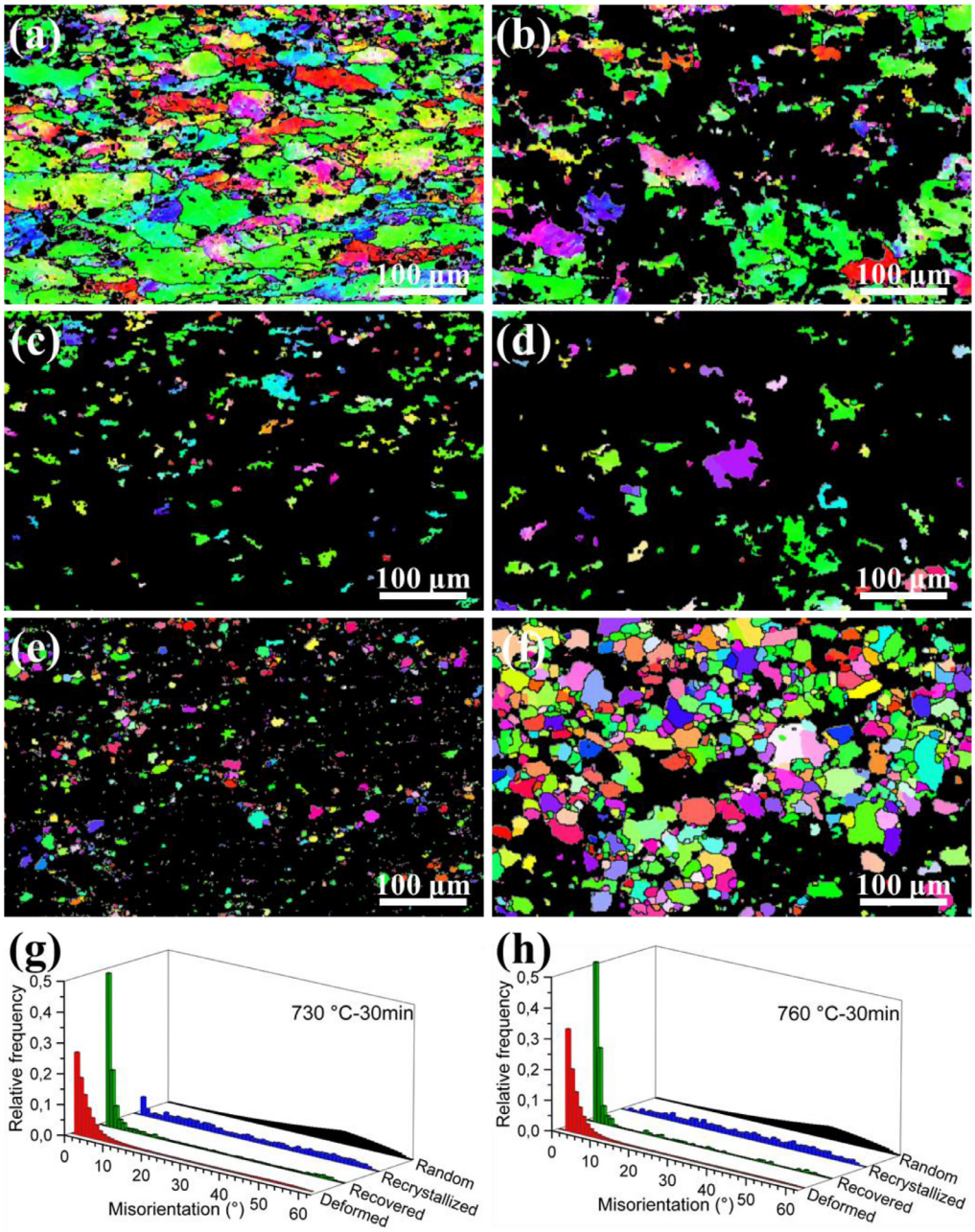

Fig. 8. Selected IPF maps of the partially recrystallized deconstructed into (a)(b) deformed, (c)(d) recovered, (e)(f) recrystallized fractions and (g)(h) misorientation distributions. Random denotes the McKenzie distribution for untextured materials.

few deformed grains remain. With the increase of annealing temperature, the recrystallization accelerated obviously, as shown in Fig. 7(e), although a short annealing time of 15 min, the area fractions of recrystallization reached 78.9%. Full recrystallization was achieved after annealing at 850 °C for 30 min. Note that the alloy was annealed at 850 °C for 480 min and 1000 °C for 30 min, the grain sizes counted from Fig. 7(h, i) were 13.8 μm and 17.1 μm, respectively, indicating that the recrystallized grains had better thermal stability at high temperature.

To investigate microstructural evolution in detail during recrystallization, we applied cut-off criterion with θ_c set to a default value of 1.0° Taking the partially recrystallized sample as an example in Fig. 7(a, b), the partially recrystallized IPF deconstructed into deformed, recovered and recrystallized fractions, as shown in Fig. 8. One of the benefits of microstructure deconstruction is that it allows individual subset to quantify the contribution of each part to the whole. Fig. 8(a, b) displays the deformed grains IPF map of the partially recrystallized samples. The deformed grains in the maps shown green color signify <110>-type orientations parallel to the RD. Significant orientation gradients were displayed within deformed grains. The orientation gradient indicated the local strain (e.g., dislocation stacking, second-phase particles pinning) in the deformed grains. As the annealing temperature increased, the nucleation sites and grain size of recrystallized grains increased significantly, as shown in Fig. 8(c) and (d). It was worth noting that the recrystallized grains or subgrains preferentially nucleated and grew at the grain boundaries. Dislocations and defects aggregate at grain boundaries with high energy storage, which accelerates the preferential nucleation of recrystallized grains. Fig. 8(g) and (h) demonstrate the misorientation angle distribution histogram for cold pilgered cladding tubes annealed at 730 °C and 760 °C, respectively. In the partially recrystallized samples, the misorientation of

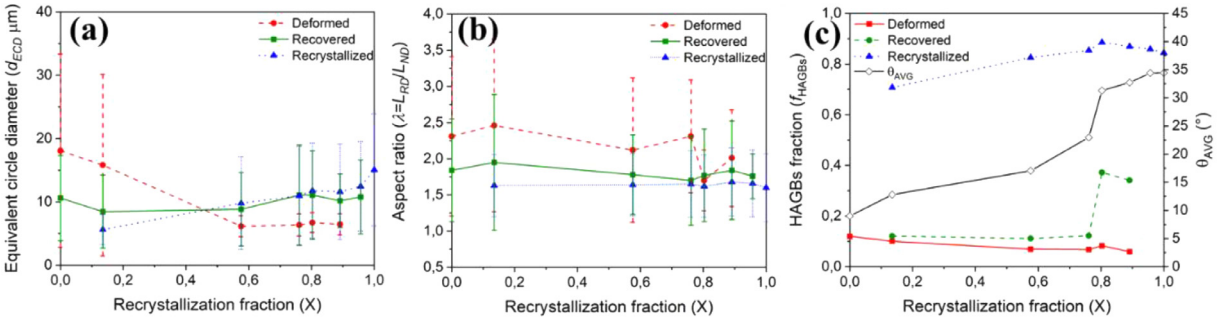

Fig. 9. Evolution of (a) equivalent circle diameter, (b) aspect ratio of grains, (c) dependence of fraction HAGBs (left axis) and average boundary misorientation (right axis) in partially recrystallized cold pilger cladding tube.

deformed grains predominates at low angles. The recovered grains mainly consist of low-angle misorientation and insignificant high-angle misorientation, indicating numerous substructures in the recovered grains. The misorientation of the recrystallized grains is distributed the entire misorientation angle, which implies that the recrystallized grains nucleate and grow. The misorientation in recrystallized grains is not a random distribution, which is caused by the LAGBs and texture from Fig. 7(a, b).

Fig. 9(a) and (b) show the average grain size and aspect ratio of specimens with different recrystallization fractions, respectively. In the early stage of recrystallization, the deformed grains show large grain size and aspect ratio. As recrystallization proceed, the error bar and equivalent circle diameter of deformed grains decreased significantly, while the recrystallized grains grow, indicating that the deformed grains are swallowed up by recrystallized grains. It is of interest that the aspect ratio of recrystallized grains remains approximately constant (λ=1.6) during recrystallization. Fig. 9(c) summarizes the HAGBs fraction and average boundary misorientation as a function of recrystallization fraction. The average boundary misorientation increases as the recrystallization fraction increases, implying that recrystallization was accomplished through the formation of HAGBs. Interestingly, the average boundary misorientation is dominated by the recrystallized grains in the early stage of recrystallization and contributed by the recovered grains in the later stage of recrystallization. The HAGBs fraction of deformed grains remains constant at a low value as the recrystallized fraction increases. Significantly increased HAGBs fraction was found in the recovered grains when the recrystallized fraction increased to 80.3% (annealed at 760 °C for 900 min). The abnormally reduced aspect ratio of deformed grains was found in Fig. 9(b). In fact, recrystallization is a thermal diffusion process through the formation and migration of HAGBs. Long-term annealing at low temperature with a small amount of remaining unrecrystallized structure due to low driving force.

3.4. Laves precipitates

Previous studies [18,24,25] reported that Laves precipitates are important for improving the microstructural thermal stability and high-temperature strength of FeCrAl alloys. Therefore, it is necessary to study the precipitation behavior of Laves phase during recrystallization. Microstructural evolution in the Laves precipitates of FeCrAl cladding tube annealed at 850 °C for different times is described based on BSE images in Fig. 10. As shown in Fig. 10(a), Laves precipitates (estimated area fraction of 3.95%) did not precipitate and coarsen in the short-time annealed (4 min) sample compared with the cold rolled microstructure (Fig. 1(a)). Deformed grain and substructure could be observed in the sample, which suggests that the alloy is undergoing recovery. As the annealing time increased to 20 min, recrystallized grains were surrounded by deformed grains, indicating that deformed microstructure was swallowed by the recrystallized Further increasing the annealing time resulted in a significant increase in the area fraction of Laves precipitates without coarsening in particle size. A small number of the equiaxed subgrain were surrounded by recrystallized grains, and high magnifications revealed a high-density of Laves precipitates in the subgrains. As the annealing time increased to 150 min, all α grains were equiaxed, indicating achieving full recrystallization. The area fraction and particle size of Laves precipitates remained stable during the annealing process. To investigate the composition of Laves phase, we performed EDS elemental mapping analysis on the white particles at the grain boundaries in Fig. 11a. The composition of the particles in Fig. 1b-f shows that the particles mainly contain Mo and Nb. The compositions of the matrix and particles were measured and listed in Table 2. References [18,19] confirmed the formation of Fe_2Nb-type Laves phase during annealing. Besides, the EBSD Kikuchi pattern of these particles were indexed, showing a Fe_2Nb-type structure. Laves phase particles contain less Cr and Al but are rich in Si compared with the matrix.

Table 2
Compositions of matrix and particles in Fig. 11(a) determined by EDS (wt%).

Location	Fe	Cr	Al	Mo	Nb	Ta	Ti	Si
Matrix	82.21	12.46	3.57	1.26	–	–	0.2	0.3
Particles	49.59	5.68	2.05	8.32	30.89	1.4	0.69	1.38

3.5. Texture evolution during annealing

Fig. 12 shows the φ_2 = 45° ODF map derived from the entire IPF map for the samples reproduced in Fig. 1(b) and Fig. 7(a~d, f~h) respectively. Based on the schematic diagram of the ideal body-centered cubic material φ_2 = 45° ODF section (Fig. 12(i)), cold pilgered sample in Fig. 12(a) exhibited typical rolling textures consisting of α-fiber and γ-fibers. A double-pole α-fiber was extended from {221}<110> to {223}<110>, while γ-fiber strong point texture component appear at {111}<110>. Partial recrystallization contributes to the α-fiber shrinking in the ⟨110⟩ invariant direction, and forms {111}<110> oriented γ-fiber. As the recrystallization fraction increases, the γ-fiber spread in the whole orientation line, but the overall texture intensity weakens slightly. In the fully recrystallized sample, the γ-fiber with orientation clusters {111}<112>.

The φ_2=45° ODF section maps shown in Fig. 12 reveal the change of crystallographic texture during recrystallization for FeCrAl cladding tube. To further quantify the evolution of texture during the recrystallization, Fig. 13 plots the area fractions of α-fiber, γ-fiber and λ-fiber components for different recrystallization fractions. In the early stage of recrystallization, α-fiber decreased

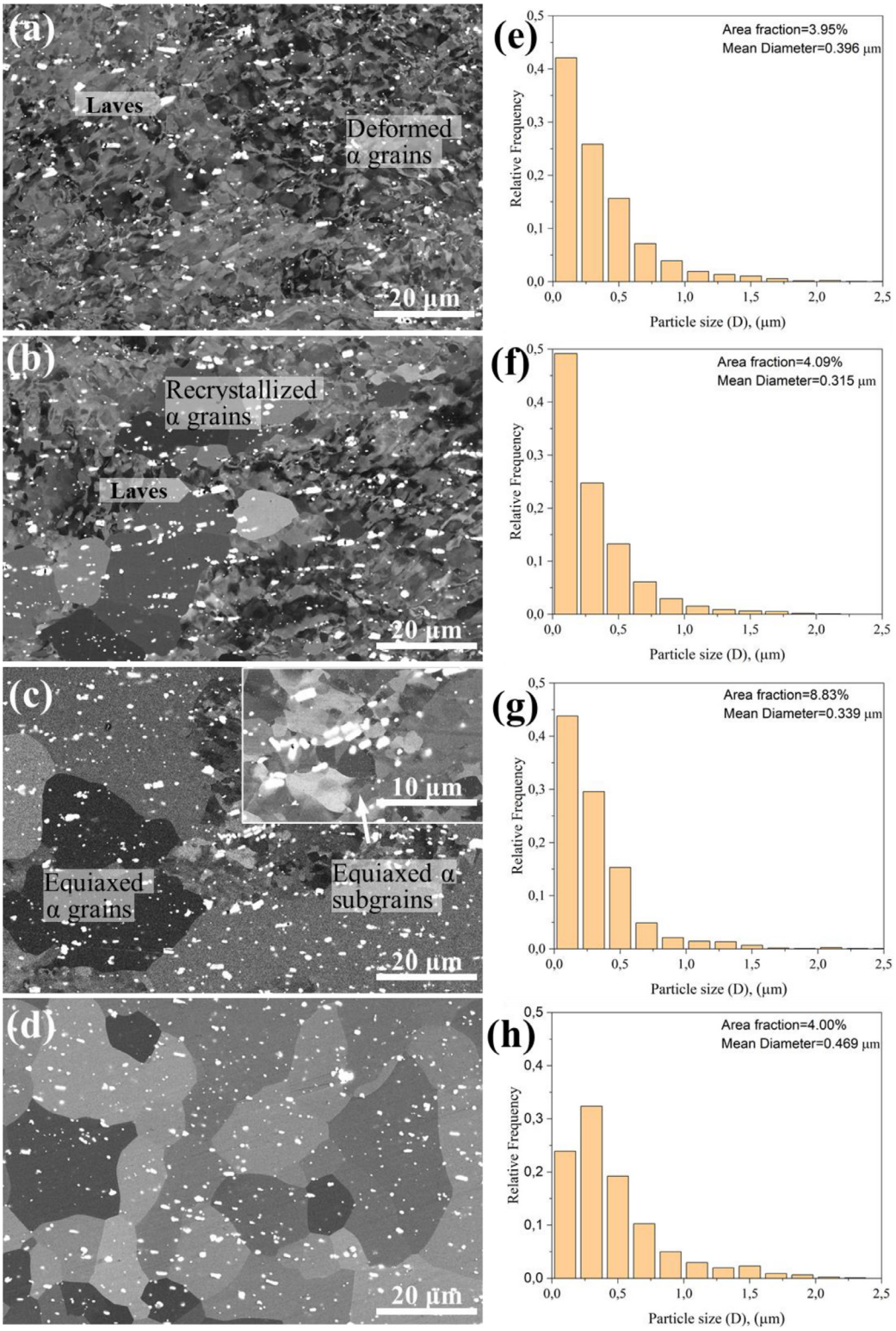

Fig. 10. BSE images revealing the Laves precipitates evolution in FeCrAl cladding tube upon annealing at 850 °C for (a)(e) 4 min, (b)(f) 20 min, (c)(g) 30 min, and (d)(h) 150 min.

significantly and γ-fiber increased, while the λ-fiber a constant. In the late stage of recrystallization, the area fractions of α-fiber, γ-fiber and λ-fiber remained constant at 50%, 14% and 6%, respectively.

The $\varphi_2 = 45°$ ODF sections of Fig. 12(b-g) were deconstructed into un-recrystallized and recrystallized subsets to discuss the contribution of each subset to texture evolution. The $\varphi_2 = 45°$ ODF sections associated with the un-recrystallized fractions of the various partially recrystallized maps after cold pilger rolling are reproduced in Fig. 14. As shown in Fig. 14(a), orientation cluster in the unrecrystallized fraction was {111}<110> texture component. The initial texture components {223}<110> and {221}<110> of α-fiber

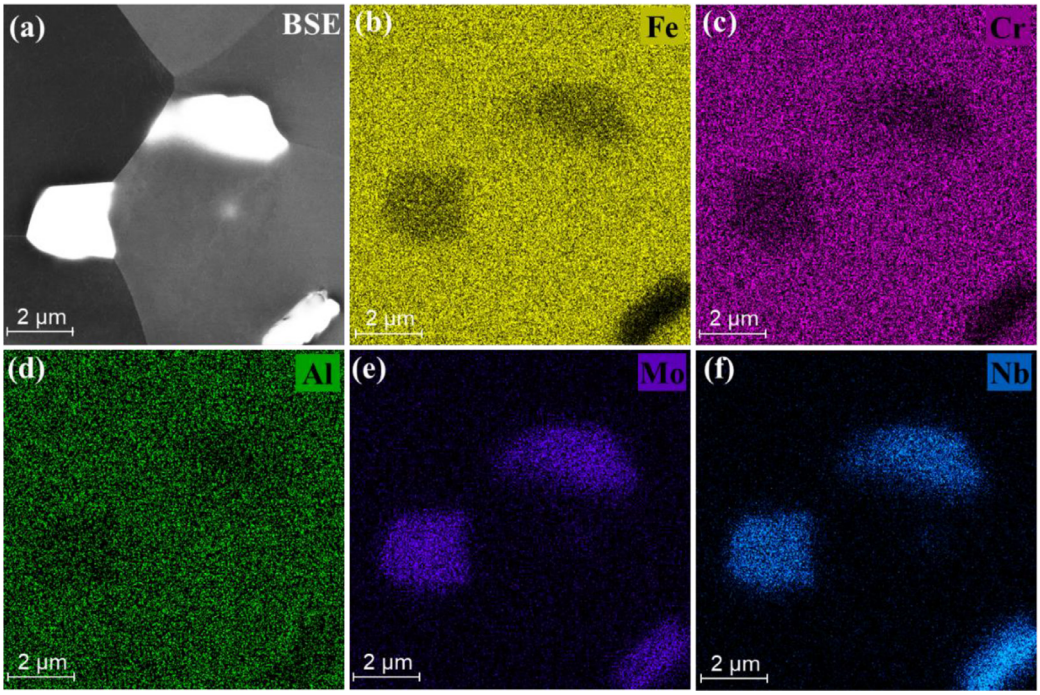

Fig. 11. (a) BSE image of FeCrAl alloy after annealing for 3 h at 850 °C. (b-f) Corresponding composition maps of Fe, Cr, Al, Mo, and Nb, respectively.

disappear, although the recrystallization fraction is only 13.5%. As recrystallization proceeds, the {111}<110> component remains stable, as shown in the unrecrystallized green grains in Fig. 7. The texture component {111}<110> belongs to {111}//ND and <110>//RD fibers, indicating that the unrecrystallized grains are located at the intersection of γ-fiber and α-fiber. In the later stage of recrystallization, the sharply decreased deformed and recovered grains resulted in an increasing overall texture density. It is well known that the $\varphi_2 = 45°$ ODF map is the cross-section map of $\varphi_2 = 45°$ in Euler space for grains with different orientations in EBSD IPF maps. A few grains in Euler space cause a strong micro-texture, which is the reason that XRD is used to measure the macro-texture.

The recrystallized fraction φ_2=45° ODF map of partially recrystallized samples was shown in Fig. 15. In the early stage of recrystallization, the low storage energy {001} orientation recrystallized grains preferentially nucleated in the deformed grains, which is related to the formation of λ-fiber in Fig. 14a. The newly nucleated grains clustered mainly around {111}<110>, although the number of grains is few (Fig. 7a). As recrystallization fraction increases, γ-fiber spread in the whole orientation lines and the overall texture density increases. In the later stage of recrystallization, the overall texture density of γ-fiber remained stable, indicating that the recrystallized γ-fiber was thermally stable.

4. Discussion

As demonstrated in Fig. 1, cold-pilgered microstructure showed heterogeneous deformed structures and <110>-orientation grains. The orientation gradient and dense network of LAGBs within deformed grains indicated large local strain and accumulation of high dislocation density in the tube. Pilger rolling is to reduce the diameter and wall of the tube blank by changing the cross-section and finally obtaining the seamless tube. The tube is subjected to not only radial strain but also axial strain during pilgering, resulting in anisotropic microstructures and highly dense substructure [26,27]. These high storage energy substructures act as potential nucleation sites and play a vital role during recrystallization. The prominent crystallographic orientation in cold-pilgered tube can be described in terms of the Taylor factor M defined in refs. [28,29]:

$$M = \frac{\delta_{ij}}{\tau_C} = \frac{\Sigma\delta\gamma_k}{\delta\varepsilon_{ij}} \tag{4}$$

where δ_{ij} represents a flow stress, τ_c is the critical resolved shear stress, and $\Sigma\delta\gamma_k$ is the sum of shear strains on given slip systems to accomplish the strain $\delta\varepsilon_{ij}$. Grains with small M values are expected to adapt more easily to the applied strain with smaller stress than grains with large M values. The mean value of M for axisymmetric deformation of body-centered cubic materials is about 3. The Taylor factor map and its $\varphi_2 = 45°$ ODF section map are shown in Fig. 16. As shown in Fig. 16(a), the λ-fiber grains have a small M value of about 2.2, while the α-fiber grains have a large M value of 3.8 ({111} <110>). Fig. 16b shows the high M-value grain distribution on the α-fiber and γ-fiber orientation lines consistent with Fig. 12a. Sun et al. [18] also reported that the orientation-dependent microstructure follows the Taylor model in deformed and annealed FeCrAl alloys.

Based on the evolution of hardness and microstructure during the annealing process, the start recrystallization temperature of the cold-pilger tube was estimated to be 730~800 °C. The recrystallization curves obtained by the microstructural and Vickers hardness approaches illustrated almost the same trend. The investigation of the recrystallization kinetics using the JMAK model showed that recrystallization was significantly fast with increasing temperature. Recrystallization is known to be affected by several factors, such as annealing temperature and cumulative deformation, nucleation and growth rate, density and distribution of nucleation sites. In this study, n and k values (see Table 1) of the alloy increased with increasing annealing temperature, indicating faster recrystallization nucleation and growth rates. The value of n between 1 and 2 indicates that the recrystallized grains are pseudo two-dimensional growth. Humphreys and Hatherly [22] reported that the lower value of n predicted by JMAK theory was due to the heterogeneity of recrystallization. Previous studies [18,19] have shown that Laves phase pinning grain boundaries increased re-

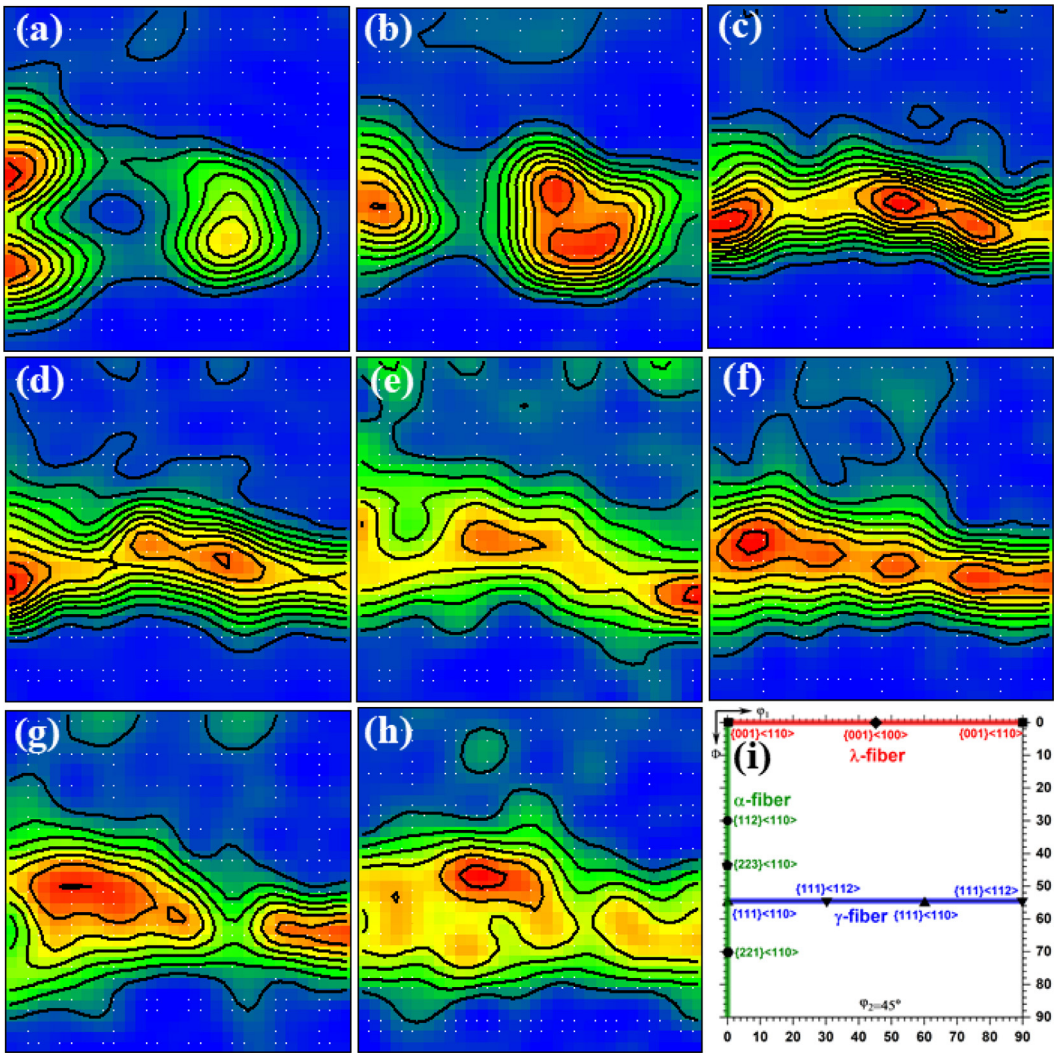

Fig. 12. φ_2 = 45° ODF section maps obtained from EBSD analysis for specimens with different recrystallized fractions, (a) Cold-pilgered sample, (b) X_{REX}=13.5%, (c) X_{REX}=57.6%, (d) X_{REX}=76.1%, (e) X_{REX}=80.3%, (f) X_{REX}=89.1%, (g) X_{REX}=95.7%, (h) X_{REX}=100% and (i) ideal body-centered cubic material. Contour levels: 1×.

crystallization temperature and recrystallization incubation period. Fig. 10 also showed that the high density of Laves precipitates aggregated at subgrain boundaries.

The recrystallization activation energy of FeCrAl cold pilgered tube was calculated to be 144.46 kJ/mol, which is approximately 1.6 times the activation energy of α-Fe grain boundary diffusion (91 kJ/mol at 873–1083 K) [30]. Liang et al. [20] reported that the apparent activation energies for recrystallization of FeCrAl alloys with cold rolling reduction ratios of 30%, 50%, and 70% were 161.385, 144.77, and 95.362 kJ/mol, respectively. The higher activation energy can be attributed to the Laves phase and high diffusion activation energy of Mo (282.6 kJ/mol [31]) and Nb (224.0 kJ/mol [32]) solute atoms in α-Fe.

IPF maps shown in Fig. 7 demonstrate the microstructural evolution during recrystallization process in cold pilgered tube. According to Sun et al. [18], the recrystallization process of FeCrAl alloy is the growth of pre-nucleated grains in the deformed structure at the expense of releasing the energy stored in the deformed matrix. A few micrometers of recrystallized grains occur at grain boundaries during annealed at 730 °C, and the recrystallization fraction is 13.5%. With the annealing temperature increasing to 760 °C, the recrystallization grains grow and the recrystallization fraction reaches 57.6%. The recrystallization fraction increases with the increase of annealing time. After 900 min isothermal annealing at 760 °C, 20% of un-recrystallized grains remain. However, when annealing at 800°C for 15 min, the recrystallization fraction of 79% is almost the same as that annealed at 760°C for 900 min, indicating that increasing annealing temperature significantly accelerates recrystallization. Full recrystallization was completed by annealing at 850 ~ 1000°C for 30 min. The growth rate of recrystallized grains can be expressed as follows [22]:

$$v = \mathrm{MF} \tag{5}$$

Where M is grain boundary mobility. F is the driving force of recrystallization. In general, F is affected by various factors such as the stored energy (E) of the deformed matrix, the retarding pressure (P_s) due to solute drag and the pinning force (F_d) of the dispersion-strengthened precipitates. E is related to orientation-dependent, and the order is $E_{110} > E_{111} > E_{211} > E_{100}$ [33,34]. It can also be seen from Fig. 7 that the <110>-oriented deformed grains store high-energy low-angle grain boundaries. As the annealing temperature increases, a higher number of nuclei can grow, resulting in an increased recrystallization fraction.

The texture development during recrystallization is generally consistent with conventionally accepted boundary mobility (M) and storage energy considerations, where {001} < {112} < {111}

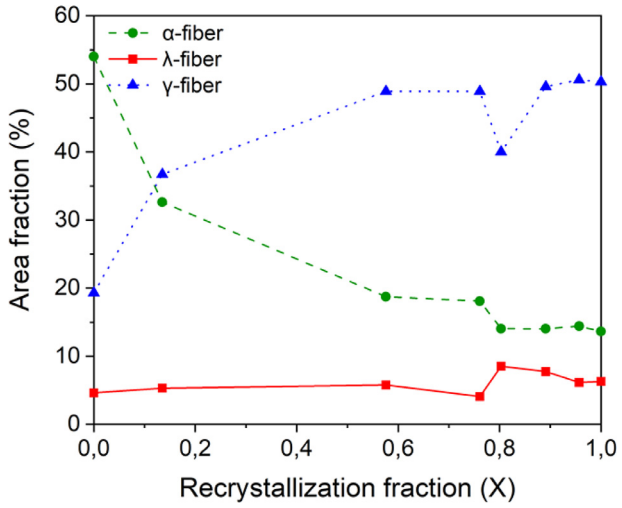

Fig. 13. Evolution of fiber texture components during recrystallization of cold pilgered cladding tubes.

< {110} orientations are ranked from lowest to highest storage energy [33,34]. The boundary mobility is temperature dependent and evaluated according to the Arrhenius-type relationship [22]:

$$M = \mathrm{M_0}\exp\left(-\frac{\mathrm{Q}}{\mathrm{RT}}\right) \tag{6}$$

Where, $\mathrm{M_0}$ as initial value, Q as the apparent activation energy for transfer of atoms across the boundary, R as the universal gas constant and T as the temperature. Boundary mobility is sensitive to both temperature and boundary characteristic. The main deformed grains in ODF map in Fig. 12(a) belongs to <110> orientation. The {001} oriented grains have lower energy and are the primary nuclei in the deformed structure at low temperatures as shown in Fig. 7a and Fig. 15a. The increase of annealing temperature leads to faster thermal diffusion of atoms, and the recrystallized grains with higher energy {111} orientations begin to grow. In the later stage of recrystallization, prominent γ-fiber is composed of {111} and ⟨110⟩ oriented grains with high storage energy. The prominent γ-fiber in FeCrAl alloy annealed tubes have excellent formability, which is of great significance in preventing premature cracking of cladding tubes during processing.

The microstructure evolution of cold-pilgered FeCrAl alloy tube is strongly controlled by annealing temperature and time. In order to achieve desirable microstructures with balanced processability and mechanical properties, optimization of processing conditions is necessary. Deformed microstructures without recrystallization could be maintained at a low annealing temperature (e.g., 700 °C); however, the low annealing temperature could result in relatively high hardness and strong deformation texture, which lead to large deformation resistance for further processing. High temperature (e.g. ≥850 °C) is easy to soften the material but rapid grain recrystallization is possible, especially when increase the temperature to obtain fully recrystallized grains takes a sharp reduction in time. When the temperature range of ~730–800 °C with 30 min dwelling period, partial recrystallization microstructure can be obtained. Hence, the study provides us balance the annealing temperature and microstructure. Higher annealing temperature is beneficial to the beginning of pilgering stage, because it needs to overcome the larger deformation resistance of the initial wall thickness reduction, while lower annealing temperature is suitable for the later stage of pilgering stage, which pays more attention to the control of the structure. In addition, the microstructure of FeCrAl alloy is also controlled by Laves precipitates. Sun et al. [18] reported that the addition of Laves particles effectively enhanced and delayed the recrystallization kinetics of FeCrAl alloy compared with base composition alloys. Therefore, the effect of the chemical composition of FeCrAl alloy should be considered in the optimization of processing conditions.

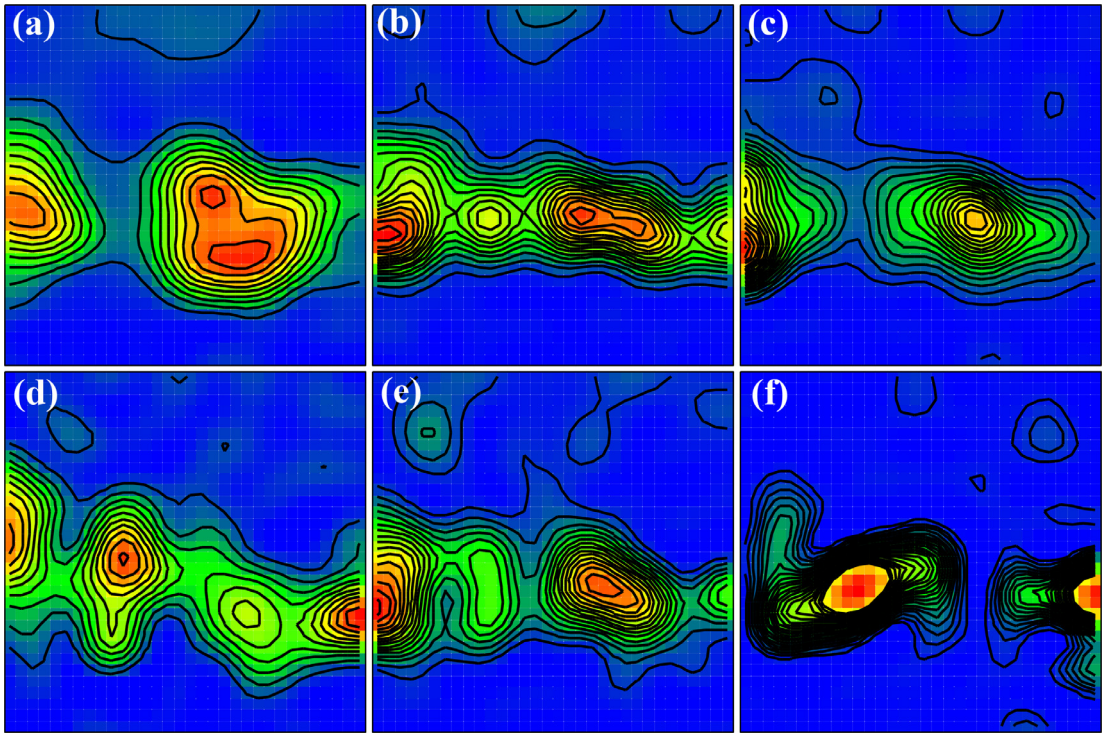

Fig. 14. φ_2 = 45° ODF maps of the un-recrystallized fraction for specimens with different recrystallized fractions, (a) X_{REX}=13.5%, (b) X_{REX}=57.6%, (c) X_{REX}=76.1%, (d) X_{REX}=80.3%, (e) X_{REX}=89.1%, (f) X_{REX}=95.7%. Contour levels: 1×.

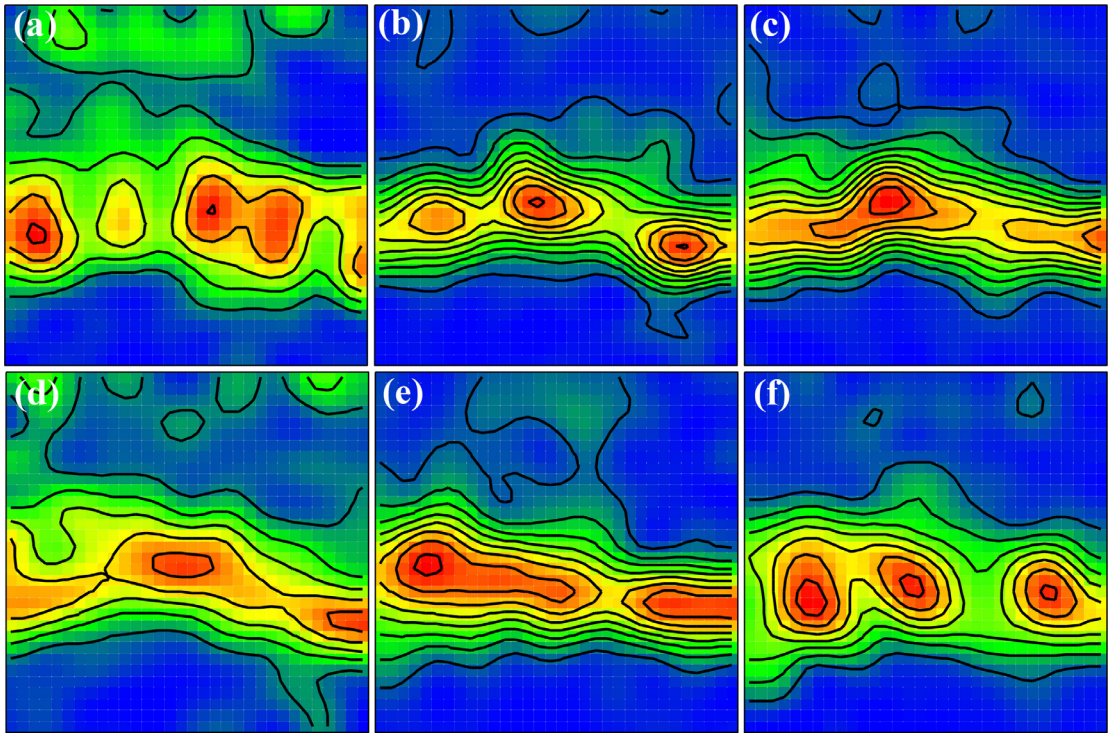

Fig. 15. φ_2 = 45° ODF section maps of the recrystallized fraction specimens with different recrystallized Please check funding information and confirm its correctness.fractions, (a) X_{REX}=13.5%, (b) X_{REX}=57.6%, (c) X_{REX}=76.1%, (d) X_{REX}=80.3%, (e) X_{REX}=89.1%, (f) X_{REX}=95.7%. Contour levels: 1×.

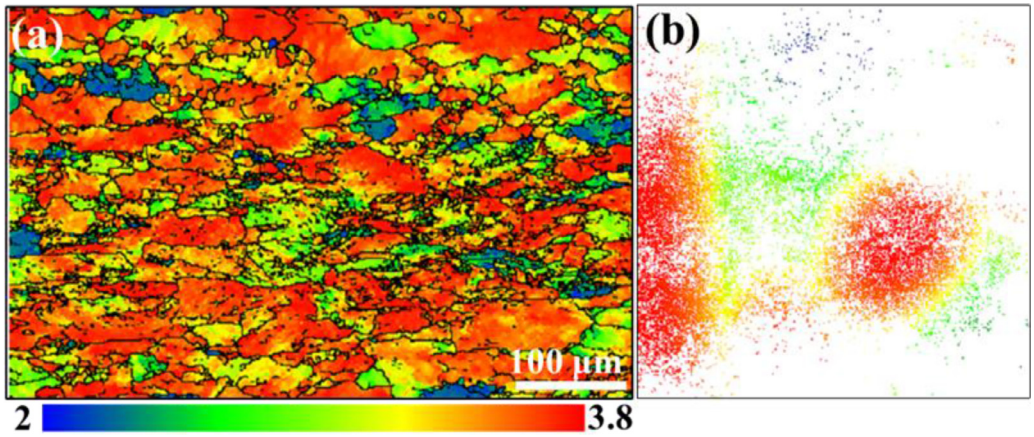

Fig. 16. (a) Taylor factor map assuming the {110}<111> slip system and (b) φ_2 = 45° ODF section map of Taylor factor. Refer to Fig. 1b for representative orientations in the map.

5. Conclusion

The recrystallization behavior of cold pilgered FeCrAl cladding tube was investigated with Vickers hardness measurements and EBSD. The conclusions were summarized as follows:

(1) Recrystallization started at the temperature range of 730~800 °°C in cold pilgered cladding tubes. The discontinuous recrystallization was observed during annealing at 730~760 °C and completed recrystallization annealed at 850~1000 °C of the cladding tube. The rate of recrystallization for the cladding tube is temperature dependent. The recrystallization kinetics of the cladding tube was quantitatively described by the JMAK equation and the recrystallization activation energy was ~144.46 kJ/mol.

(2) The partially recrystallized EBSD map based on critical internal misorientation angle was deconstructed into deformed, recovered and recrystallized grain fractions. Heterogeneous microstructures such as high aspect ratio grains and high proportion LAGBs presented in the deformed and recovered grains, and the recrystallized grains had equiaxed grains and overwhelmingly HAGBs.

(3) Cold pilgered cladding tube showed sub-micrometer Laves precipitates dispersed in the α matrix. Pinning of subgrain boundaries by Laves precipitates resulted in delaying recrystallization kinetics and stable grain size.

(4) Different from the texture of FeCrAl alloy plates (α, γ, and <100>//ND fibers) and FeCrAl-ODS alloy cold pilger cladding (strong α and γ-fibers), wrought FeCrAl alloy cold pilger cladding shows strong α-fiber. The α-fiber weaken and γ-fiber strengthen as recrystallized fraction increases. The prominent γ-fiber of recrystallized grains would be beneficial to the processability of the cladding tube.

Declaration of Competing Interest

The authors declare that they have no known competing interests or personal relationships that could have appeared to influence the work reported in this paper.

Data availability

Data will be made available on request.

Acknowledgments

This research was funded by the Key Project of Nuclear Safety and Advanced Nuclear Technology (2019YFB1901002), "the Project supported by State Key Laboratory of Powder Metallurgy", Central South University, Changsha, China.

References

[1] S.J. Zinkle, G.S. Was, Materials challenges in nuclear energy, Acta Mater 61 (2013) 735–758.
[2] L. Hallstadius, S. Johnson, E. Lahoda, Cladding for high performance fuel, Prog. Nucl. Energ. 57 (2012) 71–76.
[3] A. Zieliński, S. Sobieszczyk, Hydrogen-enhanced degradation and oxide effects in zirconium alloys for nuclear applications, Int. J. Hydrogen Energ. 36 (2011) 8619–8629.
[4] A.T. Motta, L.Q. Chen, Hydride formation in zirconium alloys, JOM 64 (2012) 1403–1408.
[5] R. Thieurmel, J. Besson, E. Pouillier, A. Ambard, A. Françoise, G. Lorenzona, Contribution to the understanding of brittle fracture conditions of zirconium alloy fuel cladding tubes during LOCA transient, J. Nucl. Mater. 527 (2019) 151815.
[6] A.T. Motta, L. Capolungo, L. Chen, Hydrogen in zirconium alloys: A review, J. Nucl. Mater. 518 (2019) 440–460.
[7] R.B. Rebak, in: Chapter 5 FeCrAl–iron–chromium–aluminum monolithic alloys, Accident Tolerant Materials for Light Water Reactor Fuels, Elsevier, 2020, pp. 83–141.
[8] Y. Yamamoto, B.A. Pint, K.A. Terrani, K.G. Field, Y. Yang, L.L. Snead, Development and property evaluation of nuclear grade wrought FeCrAl fuel cladding for light water reactors, J. Nucl. Mater. 467 (2015) 703–716.
[9] M.N. Gussev, K.G. Field, Y. Yamamoto, Design, properties, and weldability of advanced oxidation-resistant FeCrAl alloys, Mater. Design. 129 (2017) 227–238.
[10] J.P. Dong, H.G. Kim, J.Y. Park, I.J. Yang, J.H. Park, H.K. Yang, A study of the oxidation of FeCrAl alloy in pressurized water and high-temperature steam environment, Corros. Sci. 94 (2015) 459–465.
[11] P. Dong, R. Zhang, W. Hui, L. Chao, Y. Liu, Formation and stability of oxide layer in FeCrAl fuel cladding material under high-temperature steam, J. Alloy. Compd. 684 (2016) 549–555.
[12] C. Mennicke, E. Schumann, M. Ruhle, R.J. Hussey, G.I. Sproule, M.J. Graham, The effect of yttrium on the growth process and microstructure of α-Al_2O_3 on FeCrAl, Oxid. Met. 49 (1998) 455–466.
[13] V.K. Tolpygo, H.J. Grabke, Microstructural characterization and adherence of α-Al_2O_3 oxide scales on Fe-Cr-Al and Fe-Cr-Al-Y alloys, Oxid. Met. 41 (1994) 343–364.
[14] Z. Sun, H. Bei, Y. Yamamoto, Microstructural control of FeCrAl alloys using Mo and Nb additions, Mater. Charact. 132 (2017) 126–131.
[15] Y. Yamamoto, M.N. Gussev, B. Kim, T.S. Byun, Optimized Properties On Base Metal and Thin-Walled Tube of Generation II ATF FeCrAl, Oak Ridge National Laboratory, Oak Ridge, USA, 2015.
[16] N.M. George, K. Terrani, J. Powers, A. Worrall, I. Maldonado, Neutronic analysis of candidate accident-tolerant cladding concepts in pressurized water reactors Ann, Nucl. Energy. 75 (2015) 703–712.
[17] D. Pociecha, B. Boryczko, J. Osika, M. Mroczkowski, Analysis of tube deformation process in a new pilger cold rolling process, Arch. Civ. Mech. Eng. 14 (2014) 376–382.
[18] Z. Sun, P.D. Edmondson, Y. Yamamoto, Effects of Laves phase particles on recovery and recrystallization behaviors of Nb-containing FeCrAl alloys, Acta Mater 144 (2017) 716–727.
[19] Y. Zhang, H. Wang, H. Sun, G. Chen, Effects of annealing temperature on the microstructure, textures and tensile properties of cold-rolled Fe–13Cr–4Al alloys with different Nb contents, Mater. Sci. Eng. A. 798 (2020) 140236.
[20] X.L. Liang, H. Wang, Q.F. Pan, J.Y. Zheng, H.Q. Liu, R.Q. Zhang, Y. Xu, Y. Xu, D.Q. Yi, Recrystallization and mechanical properties of cold-rolled FeCrAl alloy during annealing, J. Iron Steel Res. Int. 27 (2020) 549–565.
[21] M. Dahms, H.J. Bunge, The iterative series-expansion method for quantitative texture analysis. I. General outline, J. Appl. Cryst. 22 (1989) 439–447.
[22] J. Humphreys, G.S. Rohrer, A. Rollett, Recrystallization and Related Annealing Phenomena, third Edition, Elsevier, 2017.
[23] M. Fanfoni, M. Tomellini, The Johnson-Mehl- Avrami-Kohnogorov model: A brief review, Nouv. Cim. D. 20 (1998) 1171–1182.
[24] N. Fujita, K. Ohmura, A. Yamamoto, Changes of microstructures and high temperature properties during high temperature service of Niobium added ferritic stainless steels, Mater. Sci. Eng. A. 351 (2003) 272–281.
[25] H. Wang, Y.X. Gao, M. Sun, Effects of Nb addition and heat treatment on the microstructure, mechanical property and internal friction behavior of FeCrAlMo cladding alloys, J. Nucl. Mater. 572 (2022) 154044.
[26] X. Qin, Z. Liu, H. Liu, R. Zhang, Q. Pan, Y. Wang, J. Pei, Recrystallization and texture evolution of warm-pilgered FeCrAl alloy tube during annealing at 850°C, J. Nucl. Mater. 562 (2022) 153575.
[27] S.M.S. Aghamiri, T. Sowa, S. Ukai, N. Oono, K. Sakamoto, S. Yamashita, Microstructure and texture evolution and ring-tensile properties of recrystallized FeCrAl ODS cladding tubes, Mater. Sci. Eng. A. 771 (2020) 138636.
[28]] J.F.W. Bishop, R. Hill, XLVI. A theory of the plastic distortion of a polycrystalline aggregate under combined stresses, Philos. Mag. 42 (1951) 414–427.
[29] G.I. Taylor, Plastic strain in metals, J. Inst. Met. 62 (1938) 307–324.
[30] G.E. Murch, Ferrite and austenite: diffusion, Bulk and interfacial. Encyclopedia of materials: Science and Technology, second Edition, Elsevier, 2011.
[31] H. Nitta, T. Yamamoto, R. Kanno, K. Takasawa, T. Iida, Y. Yamazaki, S. Ogu, Y. Iijima, Diffusion of molybdenum in α-iron, Acta Mater 50 (2002) 4117–4125.
[32] F. Perrard, A. Deschamps, P. Maugis, Modelling the precipitation of NbC on dislocations in α-Fe, Acta Mater 55 (2007) 1255–1266.
[33] S.H. Choi, Y.S. Jin, Evaluation of stored energy in cold-rolled steels from EBSD data, Mater. Sci. Eng. A. 371 (2004) 149–159.
[34] L. Kestens, J.J. Jonas, P. Van Houtte, Orientation selective recrystallization of nonoriented electrical steels, Metall. Mater. Trans. A. 27 (1996) 2347–2358.